Quantum Fabry-Perot Resonator: Extreme Angular Selectivity in Matter-Wave Tunneling

Constantinos Valagiannopoulos*

Department of Physics, Nazarbayev University, 53 Qabanbay Batyr Avenue, KZ-010000, Kazakhstan

(Received 28 August 2019; revised manuscript received 14 October 2019; published 18 November 2019)

The simple quantum setup of a Fabry-Perot interferometer is found to exhibit very high directional preference to impinging particle beams, with use of realistic media. Numerous optimized designs, acting as extremely sharp angular filters of matter waves, are determined by trying and testing every single combination of actual materials picked from a long list. Two types of resonances are identified whose different mechanisms are demonstrated through the spatial distribution of wave-function magnitude and probability current, while their robustness with respect to fabrication defects is also examined. Such findings offer additional degrees of freedom when designing architectures for a broad range of quantum-engineering applications that involve beam tunneling and provide a set of limits for the angular selectivity that can be achieved with the considered geometry.

DOI: 10.1103/PhysRevApplied.12.054042

I. INTRODUCTION

Quantum effects, occurring when charged particles travel in the presence of inhomogeneous matter and interactions of the developed electromagnetic fields with inclusions of various sizes, shapes, and textures, are behind multiple and diverse quantum applications. An indispensable experimental tool of modern condensed-matter physics to measure the density of electrons in a medium as a function of their energy is the scanning tunneling spectroscopy [1], being vastly based on the coupling of particle beams with metallic or superconducting samples resulting in the desired tunneling currents. Furthermore, the suitable pairing of matter waves with quantum materials constitutes the backbone of quantum sensors [2], offering high sensitivity and precision in many measuring processes of applied physics, with use of platforms like trapped ions or flux qubits. The interplay of particle dynamics with external couplings in the framework of cavity electrodynamics setups [3] or doped crystals [4], can also reveal the basic principles governing phenomena as coherence, entanglement, and nonlocality, paving the way to quantum control and quantum memory. Such physical systems making quantum interfaces between light and matter, may be additionally exploited as components in quantum networks [5], ensuring size-scaling connectivity and error-corrected teleportation of states between the nodes.

All these disruptive techniques and technologies have recently ignited enormous funding initiatives and legislative acts [6] that have followed major investments from industry giants and are expected to boost research activities pertaining to the development of alternative quantum devices over the next decade. Only during the last couple of years have the National Science Foundation (NSF), Army Research Office (ARO) and the US Department of Defense (DoD) released resources and approved several large-scale research endeavors on quantum matter incorporated in configurations supporting unconventional quantum interactions. Hybrid structures combining layers of dissimilar material classes suitable for quantum superposition [7], setups excited by high-pulsed fields to realize and manipulate new phases in strongly correlated substances [8] and quantum layouts permitting *ab initio* characterization at the atomic scale [9], are just few indicative examples.

One of the most popular geometries that quantum texture is distributed is in planar multilayers; they give uniform configurations, where quantum wells and barriers are the same across all the normal directions. They have been traditionally employed in certain experimental efforts for a variety of objectives from enhancing the tunneling current density through gallium arsenide slabs [10] and tuning electronically the reflection [11] to increasing the standing-wave contrast with low insertion loss [12] and switching the response via reflector stacks [13]. However, multilayers of quantum media possessing different potential energy levels are still used in light-emitting diodes loaded by nitride layers for color conversion [14], coupling of quantum dots with microcavities [15], and germanium-based electroabsorption modulators [16]. The quantum electrodynamic interactions have also been extensively investigated in similar planar architectures like laser diodes [17] acting as beam splitters [18] and microcavity mirrors favoring spontaneous emission [19,20].

*valagiannopoulos@gmail.com

Perhaps the simplest planar geometry is the so-called Fabry-Perot interferometer that has been initially introduced in photonic design [21]; however, it is very commonly utilized in quantum architectures where matter waves are destructively or constructively interfering to produce controllable output. One or more pairs of interfaces have been proposed since the mid-1980s for resonant tunneling of the impinging quantum particles [22] exploited in designing transistors, circuits, and logical gates [23] or used as a tuning mechanism in quantum cascade lasers [24]. The time that the particle needs in order to tunnel through a potential inhomogeneity is a critical quantity determining the performance of the associated devices; thus, it has been the topic of several studies where the role of the dwell and phase times (in analogy to wave velocities) is identified [25], while the corresponding explicit formulas are derived [26]. The concept of Fabry-Perot resonators is additionally deployed in modeling quantum cavities as couples of dissimilar mirrors useful in high-resolution length measurements [27] and oscillations between photon emission and reabsorption within the cavity [28]. Similarly, Fabry-Perot cavities have been found to support the antibunching effect for beam-distributing operation [29], ballistic electron transport in semiconductor-based configurations [30], and nonlinear light rectification for quantum optical communications [31].

In this work, we consider a planar slab of certain quantum texture and size hosted in a background medium while excited by an electron beam (e beam) impinging obliquely on its surface. The formed boundary value problem is rigorously solved like in the corresponding photonic configuration [21,32] since the governing laws (Helmholtz, Schrödinger equations) are completely analogous to each other. Indeed, there is a great variety of quantum setups that are treated in an identical way to the respective electrodynamic structures from spherical inclusions scattering, minimally [33] or maximally the matter waves [34,35], to quantum wavefront engineering prisms [36] and periodic arrays of potential barriers [37]. The basic aim of this study is to propose material combinations that exhibit extreme directional selectivity for the incident matter wave, namely block all the incoming beams except for that traveling along a specific angle. We derive the conditions under which that effect occurs and identify two distinct types of resonances leading to such a flawless outcome; to this end, a metric indicating the angular preference of the design is defined and optimized. The effective properties of numerous quantum media are compiled formulating a long directory including data from standard textbooks [38,39]; every single background and slab combination is tried and families of optimal layouts are obtained. The effectiveness of the reported structures is demonstrated by exciting them via different beams, while the sensitivities of the best-performing directional quantum filters are tested with respect to fabrication defects, inaccurate potential levels, and effective masses.

In this way, we exploit Fabry-Perot interferences of quantum particles to find numerous configurations comprising realistic media, which give an exceptionally selective angular response with increased robustness to construction imperfections. Such a library of highly performing designs gives extra degrees of freedom in the modeling and fabrication process of quantum setups serving purposes like matter-wave filtering, electron-beam steering, and quantum sensing. Importantly, it reports the limits of a simple planar configuration in terms of the directional tunneling and sets bars of selectivity performances that only more complex structures or smarter textures may pass.

II. MATHEMATICAL FORMULATION

A. Configuration and transmissivity

The analyzed geometry is depicted in Fig. 1(a), where the used Cartesian coordinate system (x, y, z) is also shown. A quantum particle traveling along an axis z with equal probability across each point of the formed normal x-y plane, meets a slab of thickness h under angle θ. Electrons in the background medium behave like they have mass $m_0 > 0$, while the level of the local potential energy is kept equal to V_0; similarly, the corresponding quantities in the material of the slab are denoted by $0 < m \neq m_0$ and $V \neq V_0$, respectively. We assume perfectly

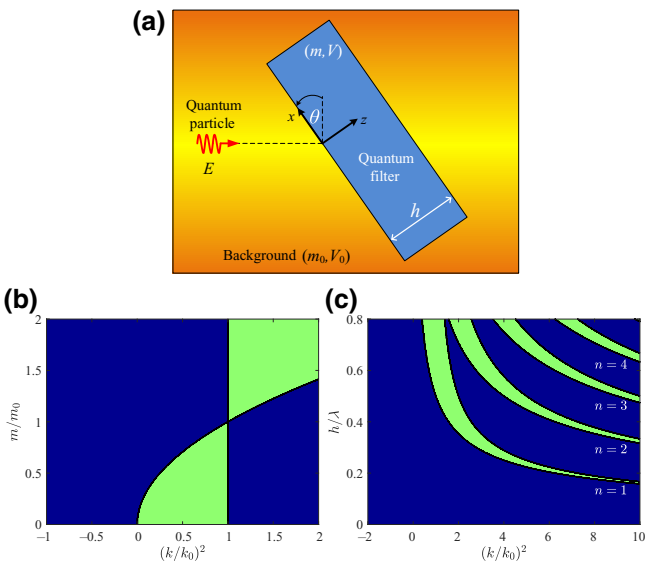

FIG. 1. (a) Configuration of the considered tilted quantum filter with an impinging matter wave traveling into a specific background. (b) Existence map (green) of the trivial matching resonance of Eq. (8) with respect to arbitrary squared wave number ratio $(k/k_0)^2$ and effective masses ratio m/m_0. (c) Existence map (green) of the Fabry-Perot resonance of Eq. (9) with respect to arbitrary squared wave number ratio $(k/k_0)^2$ and slab thickness h normalized by wavelength λ, for various orders n.

homogeneous materials ignoring imperfections and inhomogeneities on the length scale of the De Broglie wavelengths. The wave function $\Psi(\mathbf{r})$ describing the probabilistic motion of the quantum particle into an arbitrary medium with effective mass $m(\mathbf{r})$ and potential $V(\mathbf{r})$, respects the time-independent Schrödinger equation [40]:

$$\nabla\left[\frac{1}{m(\mathbf{r})}\nabla\right]\Psi(\mathbf{r})+\frac{E-V(\mathbf{r})}{\hbar^2/2}\Psi(\mathbf{r})=0, \tag{1}$$

where $\mathbf{r}$ is the related position vector, $\hbar$ is the reduced Planck constant, and E the energy of the impinging matter wave. From the fundamentals of quantum mechanics [41], we know that, with the suitable normalization, the positive quantity $\Psi(\mathbf{r})\Psi^*(\mathbf{r})=|\Psi(\mathbf{r})|^2$ is proportional to the probability of finding the electron at a point with position vector $\mathbf{r}$. In addition, the real vector,

$$\mathbf{J}(\mathbf{r})=\frac{i\hbar}{2m(\mathbf{r})}\left[\Psi(\mathbf{r})\nabla\Psi^*(\mathbf{r})-\Psi^*(\mathbf{r})\nabla\Psi(\mathbf{r})\right], \tag{2}$$

is the so-called "probability current," giving the stochastic motion direction of the quantum particle [40]; apparently, $\mathbf{J}$ is proportional to $(-\mathrm{Im}[\Psi\nabla\Psi^*])$.

Accordingly, the matter wave defining the behavior of the aforementioned particle in the absence of the inhomogeneity of the slab takes the form: $\Psi_{\mathrm{inc}}(z,x)=\exp(ik_0z\cos\theta-ik_0x\sin\theta)$, where $k_0=2\pi/\lambda=\sqrt{2m_0(E-V_0)}/\hbar$ is the wave-vector norm into the background material. However, in the presence of that thin cavity, which is supposed to work as a quantum filter, the wave function for $z<0$ changes by the reflecting-wave term $\Psi_{\mathrm{ref}}(z,x)=R(\theta)\exp(-ik_0z\cos\theta-ik_0x\sin\theta)$. In a similar manner, the entire matter wave behind the slab (for $z>h$) is given by $\Psi_{\mathrm{tran}}(z,x)=T(\theta)\exp(ik_0z\cos\theta-ik_0x\sin\theta)$, with the same wavelength λ. The functions $R(\theta),T(\theta)$ are the complex reflection and transmission coefficients, respectively. The wave function in the planar slab is written as $\Psi(z,x)=e^{-ik_0x\sin\theta}\left[A(\theta)e^{i\kappa(\theta)z}+B(\theta)e^{-i\kappa(\theta)z}\right]$, where

$$\kappa=\kappa(\theta)=\sqrt{k^2-k_0^2\sin^2\theta}, \tag{3}$$

and $A(\theta),B(\theta)$ are determinable complex functions of θ. The notation $k=\sqrt{2m(E-V)}/\hbar$ is used for the wave-vector norm in the material of the cavity.

The necessary conditions across the common boundary of two regions with effective masses $\{m_1,m_2\}$ and wave functions $\{\Psi_1,\Psi_2\}$ demand continuity of the probability amplitudes and the probability currents: $\Psi_1=\Psi_2$ and $\nabla\Psi_1/m_1=\nabla\Psi_2/m_2$. After imposing these requirements at $z=0,h$, the reflection coefficient $R=R(\theta)$ is rigorously determined as

$$R=\frac{\left[e^{2i\kappa h}-1\right](p^-)^2}{(m_0\kappa+k_0m\cos\theta)^2-e^{2i\kappa h}(m_0\kappa-k_0m\cos\theta)^2}, \tag{4}$$

where the dependencies on θ are dropped for brevity and

$$p^{\pm}=p^{\pm}(\theta)=(k^2-k_0^2)m_0^2+k_0^2(m_0^2\pm m^2)\cos^2\theta. \tag{5}$$

The transmissivity $\tau(\theta)=|T(\theta)|^2$ of the device can be computed as follows:

$$\tau(\theta)=\frac{1}{\cos^2[\kappa(\theta)h]+\left[\frac{p^+(\theta)/\kappa(\theta)}{2k_0m_0m\cos\theta}\right]^2\sin^2[\kappa(\theta)h]}. \tag{6}$$

Note that Eq. (6) holds not only when κ is real but also imaginary. Furthermore, for the special incidence angle $\sin^2\theta\to(k/k_0)^2$ that κ vanishes once $k<k_0$, the reflection and transmission coefficients tend to the following limiting values:

$$R\to\frac{1}{1+i(m_0/m)\frac{2}{\kappa_0h}},\quad T\to\frac{e^{-i\kappa_0h}}{1-i(m/m_0)\frac{\kappa_0h}{2}}, \tag{7}$$

where $\kappa_0=\sqrt{k_0^2-k^2>0}$.

Our assumption for moving particles constituting a matter wave with infinite planar extent is not unconventional; indeed, it is commonly used when modeling the excitation of quantum setups for various purposes like inclusion scattering [34] and electron manipulation [36] or even measuring effects like quantum transport [22] and resonant tunneling [23]. When it comes to how realistic is the adopted source model, one can assume that the plane wave is well mimicked by an electron beam of finite aperture being simultaneously: (i) much larger than the squared operational wavelength λ^2 to impose the field variation across many spatial periods on the front surface of the filter ($z=0$) and (ii) much smaller than the transverse size of the finite-extent slab. This condition is respected by numerous experimental endeavors including estimation of probability distributions unveiling the relaxation dynamics by a fluctuating gas considered as a one-dimensional plane wave [42] or implementation of optical lattices with a time-reversal-symmetric Hamiltonian where pairs of laser beams emulate plane waves of different frequencies [43]. Similarly, a micrometer-aperture beam is well regarded as a plane wave since it illuminates the entire plasmonic cavity to unveil the quantum regime of the tunneling occuring in it [44]. It should also be stressed that the same happens to experimental layouts of pure quantum logic, where sources of single electron guns are treated as matter plane waves [45,46].

B. Trivial and thickness resonances

We examine a particle that travels into the background medium and, accordingly, its energy should be higher than the local potential magnitude, namely $E > V_0$ (and, thus, always $k_0 > 0$). Our aim is to investigate the conditions under which a perfect matching for the incoming beam is achieved, namely a vanishing reflection: $R = 0$.

By inspection of Eq. (4), one directly observes that a trivial resonance giving zero reflecting matter wave is achieved for

$$p^-(\theta_0) = 0 \Rightarrow \cos^2\theta_0 = \frac{(k/k_0)^2 - 1}{(m/m_0)^2 - 1}, \tag{8}$$

which is not dependent on the thickness h of our quantum filter. An acceptable solution with $0 < \cos^2\theta_0 < 1$ cannot be found for $E < V$ since then k is imaginary; namely, a $k^2 < 0$ gives a fraction in Eq. (8) larger than unity. The existence of the trivial resonance in Eq. (8) is shown on the map of Fig. 1(b) by scanning the values of the squared ratio of wave numbers $(k/k_0)^2$ and effective-mass analogy m/m_0: green indicates that perfect matching may occur and blue is used for infeasible matter and particle combinations. Two parametric regions of existence are formulated around the point $(k, m) = (k_0, m_0)$ demanding proportional increase or decrease of both the examined variables $(k/k_0)^2$ and $(m/m_0)^2$. Notice that the resonance cannot be present for $k^2 < 0$, as mentioned above.

The other factor of the numerator in Eq. (4) is related to the longitudinal size h of the planar inhomogeneity and vanishes for

$$\kappa(\theta_n)h = n\pi \Rightarrow \sin^2\theta_n = \left(\frac{k}{k_0}\right)^2 - \left(\frac{n\pi}{k_0 h}\right)^2, \tag{9}$$

with $n \in \mathbb{N}^*$. These angles define the well-known Fabry-Perot resonances [21] in photonic and electromagnetic interactions, which are based on constructive and destructive interference of reflecting waves from the two interfaces of a lossless cavity. The case of $n = 0$ either corresponds to an absent slab ($h = 0$), where $\tau(\theta) = 1$ for all angles θ or to the special incident direction, yielding $\kappa(\theta) = 0$ and nonzero reflections according to Eq. (7); thus, it is not taken into account. A similar existence map to Fig. 1(b) is sketched in Fig. 1(c) but for various orders n of Eq. (9) by sweeping the ratio $(k/k_0)^2$ and the thickness h of the slab divided by the wavelength λ of the impinging matter wave. Hyperbolic shaped zones are composed, one for each order n, that overlap for thicker slabs. Furthermore, the range of h/λ leading to Fabry-Perot resonance turns narrower for increasing $(k/k_0)^2$; in contrast, when wave vectors are kept fixed, the permissible intervals of h/λ become wider for larger n. Obviously, by regulating the size h/λ, one can select which order of thickness resonance can be activated, alone or together with others, at the respective angles θ_n given by Eq. (9).

Evidently, when k is imaginary, Eq. (9) does not lead to acceptable solutions due to the "plasmonic" nature [47–49] of the slab; indeed, Fabry-Perot resonances are based on the interference of propagating and not evanescent waves [21]. Accordingly, both types of resonances allowing for $R = 0$, require a particle energy $E > \max\{V_0, V\}$; it means that unitary output $\tau = 1$ may occur for either quantum-well ($V > V_0$) or quantum-barrier ($V < V_0$) configuration. It should also be stressed that the absolute values of the energies $\{V_0, V, E\}$ do not play a role; only the relative difference between them counts. Therefore, and with no loss of generality [33–35], we can assume that the potential energy in the host medium is zero ("ground state," $V_0 \leftarrow 0$), by adjusting properly the potentials inside the material of the scatterer: $V \leftarrow (V - V_0)$. In other words, the energy of the electron $E \leftarrow (E - V_0)$ expresses its difference from the original background level V_0.

It is important to note that when considering the interface between the two media like at $z = 0$ or $z = h$, the potential-energy difference is not in general given by $(V_0 - V)$. In particular, a charge redistribution across the boundaries leads to dipole development and consequently an additional potential drop due to band offset occurs; such an effect is neglected throughout the present approach.

III. NUMERICAL SIMULATIONS

A. Optimization scheme and results

The major objective of this study is to propose simple designs like the one depicted in Fig. 1(a), that offer extremely high angular selectivity for matter waves, namely making ultra-sharp directional quantum filters. To put it alternatively, we seek thicknesses h and textures (m, V) letting ideally to pass only quantum particles (of determined energy E) that travel along an angle θ into a specific background medium (m_0, V_0), while blocking all the other directions. Given the fact that transmission of Eq. (6) always vanishes at the grazing ($\theta = \pm 90°$) angle, a good (inverse) metric for a slab acting as a filter is the average response over all possible excitation beams of quantum particles ($-90° < \theta < 90°$) defined as follows:

$$\bar{\tau} = \frac{1}{\pi}\int_{-\pi/2}^{\pi/2} \tau(\theta) d\theta. \tag{10}$$

Indeed, in a flawless scenario, $\bar{\tau} \to 0$ since $\tau(\theta) = 1$ for the perfect filtering angle and $\tau(\theta) = 0$ for all the other angles, giving a vanishing average transmissivity. Therefore, we aim at proposing combinations of $\{E, m_0, V_0, m, V, h\}$ that minimize the normalized ($0 < \bar{\tau} < 1$) quantity of Eq. (10). Note that a unitary average transmission $\bar{\tau} = 1$ corresponds to an absent slab ($h = 0$), namely the particle continues traveling uninterruptedly into the host material, regardless of the tilt θ [$\tau(\theta) = 1$ for $-90° < \theta < 90°$].

We do not consider the values of effective masses (m_0, m) and potential energies (V_0, V) as free parameters. In contrast, we formulate a long directory of realistic quantum media whose constituent characteristics are accurately measured (data are compiled from standard references [38] and recent studies [50,51]). As candidate media, we mainly regard isolated elements (IV group) and compounds (between elements of different groups III-V, II-VI); needless to say that an identical strategy for minimizing $\bar{\tau}$ applies if more complicated media like alloys, mixtures, and heterojunctions are taken into account. Our optimization approach simply tries every single pair of available materials and finds the thickness h of planar inhomogeneity maximizing the metric $1/\bar{\tau}$ each time. It should be remarked that we confine ourselves to designs that exhibit a single resonance (trivial or Fabry-Perot); structures supporting two or more angles θ of flawless transmission $\tau(\theta) = 1$ are eliminated from our contest. Such a course of action is compatible with our simple purpose: to give designs that filter all directions except for one. Obviously, if multiple fully transmissive angular zones are desirable, one can certainly include the aforementioned structures into the search scheme. In case the design supports the trivial resonance in Eq. (8), namely lies across the green regions of the map in Fig. 1(b), we deliberately choose h in order to suppress the appearance of the Fabry-Perot interference in Eq. (9). In other words, we confine our quest to the blue regions of the map in Fig. 1(b) and thus the angle $\theta = \theta_0$ at which perfect transmissivity $\tau = 1$ is recorded, is not dependent on h/λ, according to Eq. (8). Note that, even when the trivial resonance emerges, the metric $\bar{\tau}$ from Eq. (10) is a function of the thickness of the quantum filter h/λ, unlike the angle θ_0 at which $\tau(\theta_0) = 1$ is achieved.

To execute systematically the described optimization scheme, we assign to each of the considered quantum material an integer serial number $u = 1, \ldots, U$ in ascending order of V. In this way, the list of U available media gets sorted by increasing potential energy within their own volume (either playing the role of host V_0 or filter V). For a particle of specific energy level E and by trying all possible combinations of media (from the total $U \times U = U^2$ ones), we search within a wide range of slab thicknesses $0 < h/\lambda < 5$ to maximize the quantity $1/\bar{\tau}$, provided the fact that $\tau(\theta)$ takes unitary value at exactly one angle $0 < \theta < 90°$. In this way, we store for each pair of materials the optimal thickness h/λ and the achieved maximal scores; accordingly, a library of optimal configurations is formulated, which can be useful when designing quantum filters with extreme angular selectivity. Our work has a fundamentally different objective than other seemingly similar studies elaborating analogous photonic systems [52] or utilizing approximate solutions in rectangular potential barriers [53].

As noted above, the quantum materials are characterized by two effective quantities: the potential energy V defining the work functions of the texture, namely, the minimal energy needed to extract an electron from the medium into vacuum and the effective mass m, which is related to the slope of the bands for Floquet-Bloch [54] waves created into periodic crystalline texture. In contrast, when one regards the same effect in photonics, the interaction of matter with light is described in most cases through one only parameter: permittivity; indeed it is rare to find available media hosting magnetization, especially at the visible or THz regimes. That makes a big difference since in quantum setups of different effective masses ($m_1 \neq m_2$, like in our case), a discontinuity at the normal derivative of the wave function across a boundary ($\nabla\Psi_1/m_1 = \nabla\Psi_2/m_2$) is imposed, which favors the abrupt change with respect to incidence angle θ.

In Fig. 2, we illustrate the optimization results for various energy levels E of the impinging particle. Each of the presented panels possesses $U^2 = 32^2 = 1024$ pixels corresponding to the background and filter combinations of available quantum media, while the represented quantity is our maximal (with respect to $0 < h/\lambda < 5$) metric $1/\bar{\tau}$ in dB. As shown in the labels of Fig. 2, the vertical axis corresponds to the serial number u of the material used as the background host, while the horizontal axis to the medium of the filtering cavity. Only optimal designs with

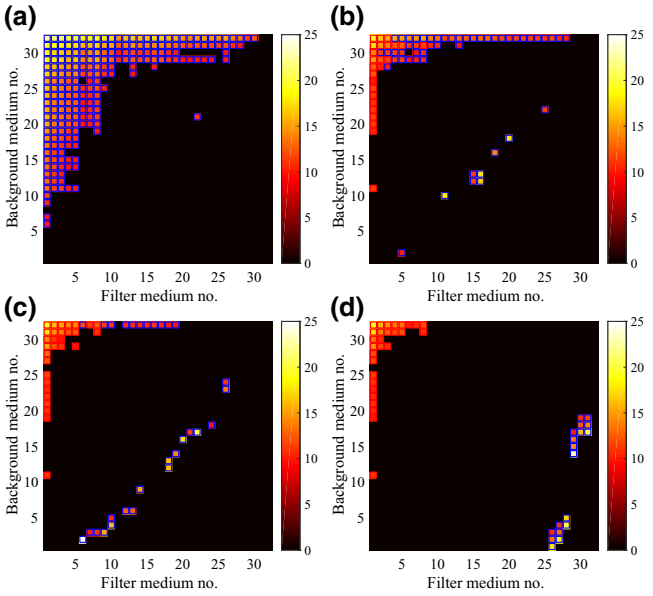

FIG. 2. Metric $1/\bar{\tau}$ in dB maximized with respect to thickness h/λ for each combination of the used quantum media. The horizontal axis corresponds to the serial number of material filling the slab and the vertical to the serial number of material used for the background host. Only results for $\bar{\tau} < 0.1$ ($1/\bar{\tau} > 10$ dB) are depicted and different quantum particle energies are considered: (a) $E = 0.1$ eV, (b) $E = 0.5$ eV, (c) $E = 1$ eV, (d) $E = 5$ eV. Red frames indicate optimization leading to trivial resonance of Eq. (8) and blue frames correspond to optimal Fabry-Perot resonance of Eq. (9).

$\bar{\tau} < 0.1 \Rightarrow 1/\bar{\tau} > 10$ dB are depicted, while the nature of resonance leading to the aforementioned optimized architectures is indicated by the color of each pixel frame: red for trivial resonance of Eq. (8) and blue for Fabry-Perot resonance of Eq. (9). Black pixels appear for one of the following reasons: (i) the maximal performance $1/\bar{\tau}$ of the device is lower than the threshold of 10 dB, which is posed to offer a clearer picture of the derived results by excluding some of the most poorly performing designs. (ii) The material of the slab is the same to the background host and thus no transmission selectivity is achieved: $\tau(\theta) = 1 \ \forall\theta \in [-90^\circ, +90^\circ] \Rightarrow \bar{\tau} = 1 \Rightarrow 1/\bar{\tau} = 0$ dB (minor diagonals of the panels in Fig. 2). (iii) The combination of quantum media and energy of the incoming electrons E is infeasible, namely our parametric point belongs at the blue regions of the existence maps of both the investigated resonances [Figs. 2(b) and 2(c)], for all the regarded $h/\lambda \in [0, 5]$. (iv) The corresponding design supports both the trivial resonance [at θ_0 from Eq. (8)] and one or more (or just more than two) of the thickness resonances [at θ_n from Eq. (9)] for all the considered h/λ; indeed, one should not forget that we are seeking transmissivity $\tau(\theta)$ profiles from Eq. (6), with a single global maximum $\tau = 1$ at a specific angle θ.

As stated above, the serial number u assigned to each quantum medium characterizes the relative position of its own potential energy V in ascending order, amongst all the $U = 32$ considered materials. Therefore, the lower right part of each panel corresponds to quantum-barrier configurations ($V > V_0$), while the upper left portion describes quantum wells ($V < V_0$). As far as the total number of available media U is concerned, it can be apparently increased in case additional textures are enlisted.

In Fig. 2(a), we consider a very low energy $E = 0.1$ eV for the impinging particle giving very large wavelengths λ for the formulated matter waves. First of all, huge magnitudes of $1/\bar{\tau}$ are recorded for a variety of material combinations, showing extreme directional preference of the tunneling through the slab. We also notice that such a characteristic favors the emergence of Fabry-Perot interference since all the frames of the reported maxima are blue. It should be mentioned that highly selective transmission is not feasible for quantum-barrier setups but only for quantum wells; indeed, as indicated above, $k > 0$ is a necessary demand for the resonances Eqs. (8), (9), which is not easily fulfilled for a tiny E when $V > V_0$. Note that the best performances are perceived for the maximal contrast $(V_0 - V)$ at the upper left region of the regarded panel.

In Fig. 2(b), the energy of the incident electrons is five times larger than that in Fig. 2(a), namely $E = 0.5$ eV. Clearly fewer designs surpass the 10-dB score threshold compared to Fig. 2(a) and, most importantly, several of them are working via the trivial resonance mechanism (red frames). It is also noteworthy that they appear in a coherent way, across slab materials possessing particularly low V; when it comes to the competing mechanism of thickness-dependent matching, it appears mainly for backgrounds of the most substantial V_0. The highest scores ($1/\bar{\tau} > 150$) are achieved again with the Fabry-Perot resonance but, surprisingly, for pairs of materials with similar potential ($V \cong V_0$), namely across the minor diagonal of the panel.

In Fig. 2(c), the level of energy for the impinging particle gets further increased ($E = 1$ eV) and the outcome of the optimal layout quest is presented. We notice that the "migration" of the designs due to thickness resonances from the upper left region of the map towards the diagonal continues. Such a trend is also demonstrated by Fig. 2(d), where the energy of the quantum particle is very high $E = 5$ eV, yielding tiny operational

TABLE I. Minimal average transmissivity $\bar{\tau}$ supporting a single Fabry-Perot resonance at $\theta = \theta_n$ according to Eq. (9), through a planar slab (different columns) of thickness h into background hosts (different rows). The energy of the impinging particle is small: $E = 0.1$ eV as in Fig. 2(a).

$E = 0.1$ eV	Indium Antimonide (InSb)	Indium Arsenide (InAs)	Gallium Antimonide (GaSb)	Indium Phosphide (InP)	Gallium Arsenide (GaAs)	Cadmium Telluride (CdTe)	Cadmium Selenide (CdSe)
Diamond	$1/\bar{\tau} \cong 174$ $h \cong 8.10$ nm $\theta \cong 47.8^\circ$	$1/\bar{\tau} \cong 134$ $h \cong 12.1$ nm $\theta \cong 45.1^\circ$	$1/\bar{\tau} \cong 105$ $h \cong 16.1$ nm $\theta \cong 44.1^\circ$	$1/\bar{\tau} \cong 65$ $h \cong 19.1$ nm $\theta \cong 48.5^\circ$	$1/\bar{\tau} \cong 74$ $h \cong 18.9$ nm $\theta \cong 44.7^\circ$	$1/\bar{\tau} \cong 59$ $h \cong 19.1$ nm $\theta \cong 48.6^\circ$	$1/\bar{\tau} \cong 50$ $h \cong 19.2$ nm $\theta \cong 53.1^\circ$
Boron Nitride (BN)	$1/\bar{\tau} \cong 90$ $h \cong 7.60$ nm $\theta \cong 48.8^\circ$	$1/\bar{\tau} \cong 77$ $h \cong 11.2$ nm $\theta \cong 44.7^\circ$	$1/\bar{\tau} \cong 59$ $h \cong 14.8$ nm $\theta \cong 44.4^\circ$	$1/\bar{\tau} \cong 39$ $h \cong 20.1$ nm $\theta \cong 43.8^\circ$	$1/\bar{\tau} \cong 42$ $h \cong 18.3$ nm $\theta \cong 42.6^\circ$	$1/\bar{\tau} \cong 36$ $h \cong 20.7$ nm $\theta \cong 43.8^\circ$	$1/\bar{\tau} \cong 31$ $h \cong 21.7$ nm $\theta \cong 44.0^\circ$
Magnesium Oxide (MgO)	$1/\bar{\tau} \cong 71$ $h \cong 17.0$ nm $\theta \cong 45.2^\circ$	$1/\bar{\tau} \cong 52$ $h \cong 24.2$ nm $\theta \cong 43.3^\circ$	$1/\bar{\tau} \cong 39$ $h \cong 31.1$ nm $\theta \cong 43.8^\circ$	$1/\bar{\tau} \cong 23$ $h \cong 32.1$ nm $\theta \cong 49.6^\circ$	$1/\bar{\tau} \cong 26$ $h \cong 32.4$ nm $\theta \cong 47.5^\circ$	$1/\bar{\tau} \cong 20$ $h \cong 32.1$ nm $\theta \cong 50.4^\circ$	$1/\bar{\tau} \cong 17$ $h \cong 32.1$ nm $\theta \cong 54.8^\circ$
Beryllium Selenide (BeSe)	$1/\bar{\tau} \cong 52$ $h \cong 17.9$ nm $\theta \cong 45.8^\circ$	$1/\bar{\tau} \cong 38$ $h \cong 25.4$ nm $\theta \cong 44.1^\circ$	$1/\bar{\tau} \cong 28$ $h \cong 31.7$ nm $\theta \cong 42.3^\circ$	$1/\bar{\tau} \cong 16$ $h \cong 36.3$ nm $\theta \cong 46.2^\circ$	$1/\bar{\tau} \cong 19$ $h \cong 36.4$ nm $\theta \cong 42.2^\circ$	$1/\bar{\tau} \cong 15$ $h \cong 36.6$ nm $\theta \cong 45.5^\circ$	$1/\bar{\tau} \cong 12$ $h \cong 36.3$ nm $\theta \cong 49.7^\circ$

wavelengths λ. It is noticeable that all the configurations with large differences $(V_0 - V)$ support trivial resonances, while the most successful regimes are sustained for quantum-barrier configurations.

Selected Fabry-Perot optimal setups from Fig. 2(a) ($E = 0.1$ eV) are presented in Table I, where each row corresponds to the same background medium (m_0, V_0) and each column to the same slab filling substance (m, V); in each box, we include the performance $1/\bar{\tau}$, the optimal thickness h of the quantum filter, and the angle θ at which $\tau(\theta) = 1$ occurs. Again, we notice that high scores $(1/\bar{\tau} > 50)$ are reported for a variety of different material pairs and thus additional degrees of freedom are offered in engineering the analyzed ultra-selective quantum filter. The best results are noted when diamond hosts the slabs due to its giant potential energy V_0; for similar reasons, diamond-based devices are designed for several quantum applications [55,56]. It is also noteworthy that the large difference between the potentials $(V_0 - V)$ makes a prerequisite for obtaining ultra-efficient Fabry-Perot interference, while the angles at which perfect transmission is achieved are found close to $\theta \cong 45^\circ$. As far as the thickness h of the slab is concerned, it is of nanometer size and thus feasible for fabrication [16,19].

In Table II, we show some representative designs, which are based on the trivial resonance mechanism of Eq. (8) at energy particle $E = 1$ eV, namely a certain part of Fig. 2(c). As indicated by the red-framed pixels of Fig. 2(c), the scores $1/\bar{\tau}$ are not very high and such a fact is reflected in Table II; nonetheless, several filters like indium antimonide into diamond perform very well. Importantly, the optimal angles exhibit a large variation across the investigated designs unlike the Fabry-Perot resonant structures of Table I. Furthermore, due to the increased energy, which makes wavelength λ smaller compared to Table I, the thicknesses get shrunk to the level of 1 nm; however, even these sizes are also realistic in manufacturing the related quantum configurations [22,23].

B. Angular and energy selectivity

In Sec. III A, we show the results of the optimization process when detecting ultra-selective tunneling designs with respect to the incidence angle of matter waves. In this subsection, we demonstrate the selectivity for some of the most highly performing configurations by observing how narrow the peaks of the output are.

In Fig. 3(a) we depict the variation of $\tau(\theta)$ with respect to the direction θ of the impinging particle for certain optimal designs of the first row of Table I; therefore, the host medium is diamond and the energy of the matter wave low ($E = 0.1$ eV). We notice that apart from the very abrupt primary peak at angles $40^\circ < \theta < 50^\circ$, a secondary local maximum appears at the normal incidence ($\theta = 0$); however, it is very small: $\tau(0) < 0.01$. One also clearly observes that the sharper resonances lead to higher performances $1/\bar{\tau}$ as indicated by Table I. In Fig. 3(b), we represent the transmission responses again for the Fabry-Perot resonant systems of Table I but regarding the designs of its second row (boron nitride host). Similar graph shapes like in Fig. 3(a) are formed but the peaks are less abrupt, a feature reflecting the lower scores $1/\bar{\tau}$ of the corresponding setups. As imposed by Eq. (6) and also shown in Fig. 3(a), the transmissivities vanish at the grazing angle ($\theta = 90^\circ$), while this time the best-performing structure in terms of $1/\bar{\tau}$ (InSb in diamond), exhibits the worst behavior for normally incident waves [highest $\tau(0)$].

In Fig. 4, we regard designs with increased particle energy $E = 1$ eV. In particular, in Fig. 4(a) we depict the variation of $\tau = \tau(\theta)$ for the best three filters from Fig. 2(c) working with the trivial resonance of Eq. (8) based on the very large host and slab difference in potential energies $(V_0 - V)$. Once again, we notice the huge selectivity of the reported layouts (with performances $1/\bar{\tau} > 40$); in particular, the InSb filter into diamond lets less than 1% of the energy pass when excited at directions different than tunneling angle $\theta_0 \cong 27.2^\circ$ at which $\tau(\theta_0) \cong 1$. In Fig. 4(b), we pick the three leading setups operating

TABLE II. Minimal average transmissivity $\bar{\tau}$ supporting exclusively a trivial resonance at $\theta = \theta_0$ according to Eq. (8), through a planar slab (different columns) of thickness h into background hosts (different rows). The energy of the impinging particle is high $E = 1$ eV as in Fig. 2(c).

$E = 1$ eV	Indium Antimonide (InSb)	Indium Arsenide (InAs)	Indium Nitride (InN)	Gallium Antimonide (GaSb)	Germanium	Boron Arsenide (BAs)
Diamond	$1/\bar{\tau} \cong 84$ $h \cong 1.09$ nm $\theta \cong 27.2^\circ$	$1/\bar{\tau} \cong 43$ $h \cong 0.80$ nm $\theta \cong 38.2^\circ$	$1/\bar{\tau} \cong 34$ $h \cong 0.71$ nm $\theta \cong 43.4^\circ$	$1/\bar{\tau} \cong 26$ $h \cong 0.61$ nm $\theta \cong 51.2^\circ$	$1/\bar{\tau} \cong 26$ $h \cong 0.63$ nm $\theta \cong 50.1^\circ$	$1/\bar{\tau} \cong 19$ $h \cong 0.55$ nm $\theta \cong 59.4^\circ$
Boron Nitride (BN)	$1/\bar{\tau} \cong 59$ $h \cong 1.43$ nm $\theta \cong 22.8^\circ$	$1/\bar{\tau} \cong 30$ $h \cong 1.03$ nm $\theta \cong 31.4^\circ$	$1/\bar{\tau} \cong 24$ $h \cong 0.93$ nm $\theta \cong 35.2^\circ$	$1/\bar{\tau} \cong 18$ $h \cong 0.81$ nm $\theta \cong 40.6^\circ$	$1/\bar{\tau} \cong 18$ $h \cong 0.82$ nm $\theta \cong 39.7^\circ$	$1/\bar{\tau} \cong 13$ $h \cong 0.74$ nm $\theta \cong 44.5^\circ$
Silicon Carbide (SiC)	$1/\bar{\tau} \cong 33$ $h \cong 1.45$ nm $\theta \cong 29.2^\circ$	$1/\bar{\tau} \cong 17$ $h \cong 1.04$ nm $\theta \cong 40.9^\circ$	$1/\bar{\tau} \cong 13$ $h \cong 0.93$ nm $\theta \cong 46.2^\circ$	$1/\bar{\tau} \cong 10$ $h \cong 0.81$ nm $\theta \cong 54.6^\circ$	$1/\bar{\tau} \cong 10$ $h \cong 0.82$ nm $\theta \cong 53.2^\circ$	$1/\bar{\tau} \cong 7$ $h \cong 0.75$ nm $\theta \cong 61.3^\circ$

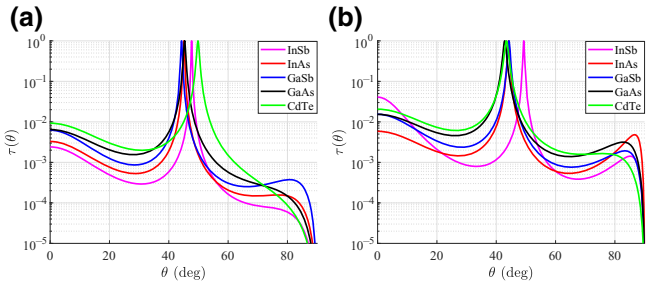

FIG. 3. The transmissivity $\tau(\theta)$ as function of the incidence angle θ for slabs of various textures from Table I ($E = 0.1$ eV) with: (a) diamond host, (b) boron nitride host. Fabry-Perot resonances occur.

via thickness resonances; they happen at mild quantum-barrier configurations with moderate difference $(V - V_0)$. One clearly remarks that the optimal directions θ_n are close to the normal one; most importantly, the investigated designs practically block every e beam with $\theta > 20°$. In particular, the InP chunk hosted in InAs makes an ultra-efficient angular filter despite its relatively increased transmissivity at normal incidence $[\tau(0) > 0.01]$.

In Fig. 5, we consider four structures supporting extremely sharp resonances with respect to incidence direction of the quantum particle and represent the transmissivity τ in contour plot as a function of the angle θ and across a range of 1 eV for the energy particle E around its optimal level. In Fig. 5(a), we consider a scenario of a low-energy particle ($E = 0.1$ eV) interacting with a slab supporting Fabry-Perot tunneling [picked from the panel of Fig. 2(a)]. One directly notes the multiple branches of unitary response formulated in a similar pattern like the existence domains of Fig. 1(c). Once the energy E of the incident electron gets increased, additional resonances emerge and $\tau(\theta) = 1$ condition is fulfilled for more than one angle θ. As indicated by the white dashed line, the minimal $\bar{\tau}$, and accordingly the narrower single peak, is achieved at an energy slightly lower than that permitting a second Fabry-Perot resonance to appear.

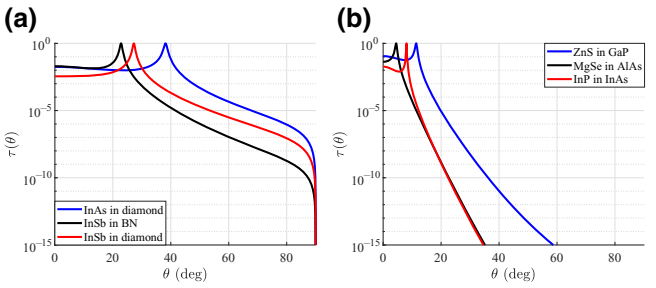

FIG. 4. Transmissivity $\tau(\theta)$ as a function of the incidence angle θ for the most successful designs of Fig. 2(c) ($E = 1$ eV) based on (a) trivial resonances (also shown in Table II) and (b) Fabry-Perot resonances.

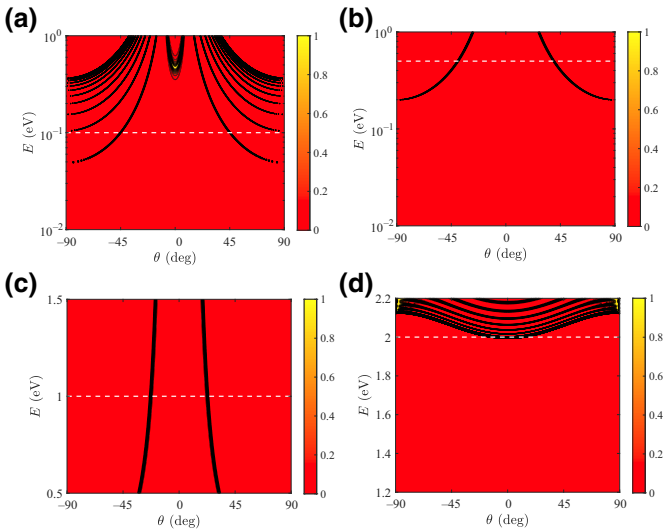

FIG. 5. Transmissivity τ with respect to matter-wave direction θ and particle energy E for (a) InAs in diamond with $E = 0.1$ eV (Fabry-Perot resonance, Table I), (b) InSb in diamond with $E = 0.5$ eV (trivial resonance), (c) InSb in BN with $E = 1$ eV (trivial resonance, Table II), (d) CdO in InSb with $E = 2$ eV (Fabry-Perot resonance). White dashed lines denote the optimal level of operational energy E.

In Fig. 5(b), a particle of $E = 0.5$ eV is examined when impinged on an optimal slab working at the trivial resonance regime [as reported by Fig. 2(b)] in a quantum-well configuration. It is natural that only one perfect transmission locus, with hyperbolic shape resembling the ones of Fig. 5(a) is created. We also remark that θ_0 becomes smaller (closer to the normal direction) as E grows, since $(k/k_0)^2$ is a decreasing function of E tending to m/m_0 for $E \to +\infty$; thus, $|\theta_0|$ shrinks, according to Eq. (8), since $m_0 > m$ and $V_0 > V$. In Fig. 5(c), we again regard a setup based on thickness-independent matching for a matter wave with $E = 1$ eV [selected from Fig. 2(c)]. It is remarkable that the flawless transmission occurs practically for the same ray θ_0 regardless of the incident particle energy; in this way, wide-band-filtering operation is sustained. In Fig. 5(d), we investigate a particle of $E = 2$ eV dealing with a Fabry-Perot resonant filter making a potential barrier. Multiple zones of resonances are created but have parabolic shape, unlike those in Fig. 2(a); however, the larger performance $1/\bar{\tau}$ is again attained at the maximum E leading to a single peak. It is finally noticeable that when E enlarges, certain islets of significant wide-angle transmission emerge, close to grazing angle $\theta \to \pm 90°$.

C. Probability amplitude and current

Apart from the transmission variation with respect to the incidence direction, it would be meaningful to represent the solution on the spatial plane (z, x) in order to understand the influence of the quantum tunneling filter on the

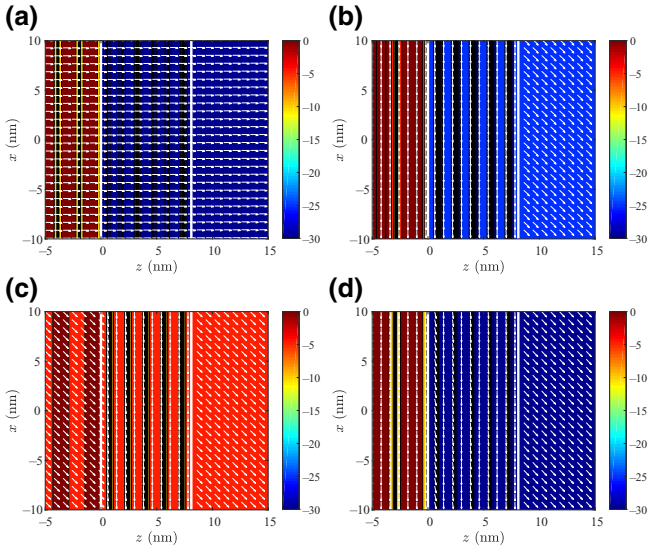

FIG. 6. Spatial distribution of the probability $|\Psi(z,x)|^2$ in dB and probability current arrows $\mathbf{J}(z,x)$ for different incidence angles: (a) $\theta = 0$, (b) $\theta = \theta_n - 2^\circ$, (c) $\theta = \theta_n$, (d) $\theta = \theta_n + 2^\circ$. Fabry-Perot resonance of an InSb slab in diamond illuminated by particle of $E = 0.1$ eV (Table I). Vertical white lines denote the boundaries of the planar filter. Plot parameters, $\theta_n \cong 47.8^\circ$, $1/\bar{\tau} \cong 174$.

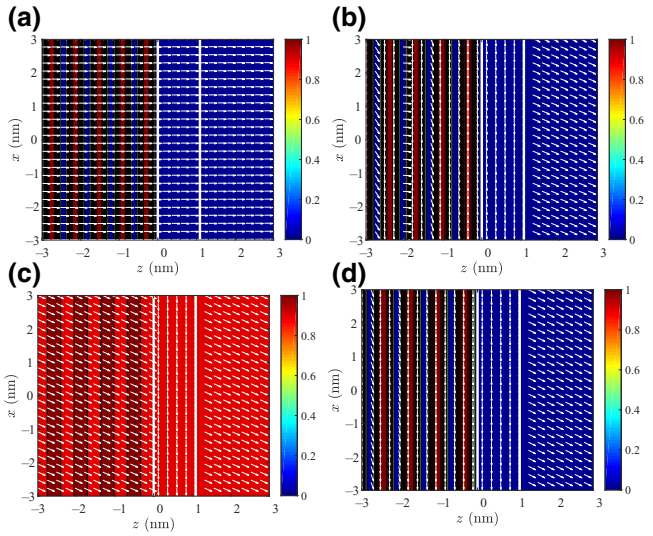

FIG. 7. Spatial distribution of the probability $|\Psi(z,x)|^2$ and probability current direction $\mathbf{J}(z,x)$ for different incidence angles: (a) $\theta = 0$, (b) $\theta = \theta_0 - 2^\circ$, (c) $\theta = \theta_0$, (d) $\theta = \theta_0 + 2^\circ$. Trivial resonance of an InSb slab in diamond illuminated by particle of $E = 1$ eV (Table II). Plot parameters, $\theta_0 \cong 27.2^\circ$, $1/\bar{\tau} \cong 84$.

impinging e beams. In Fig. 6, we choose a specific optimal design from Table I (InSb slab in diamond) and show the spatial distribution of the probability $|\Psi(z,x)|^2$ in dB; on top of it, a vector field indicates the associated probability current $\mathbf{J}(z,x)$. In Fig. 6(a), the normal incidence scenario is regarded and we can clearly notice that the magnitude of the transmissive probability is negligible for $z > h$, while the direction is always towards the $(+z)$ axis. We also examine the cases [Figs. 6(b) and 6(d)] of illuminating the quantum filters at angles slightly $(\pm 2^\circ)$ different than the resonant one θ_n, as dictated by Eq. (9). Again, the response is particularly low, while the direction of the particle into the slab is parallel to the $(-x)$ axis and standing-matter waves are formed for $z < 0$. In Fig. 6(c), we consider the optimal excitation case $(\theta = \theta_n)$ and a flawless transmission is recorded; note that no reflections occur for $z < 0$ since the current $\mathbf{J}(z,x)$ fully retains its incidence ray θ_n.

The high angular preference of the proposed designs is also demonstrated by Fig. 7, where another optimal structure with the same materials but based on trivial resonance is considered ($E = 1$ eV from Table I). Obviously, the operational wavelength λ is smaller compared to Fig. 6 and, accordingly, the whole design shrinks. For this reason, the slab is thinner and the probability $|\Psi(z,x)|^2$ is homogeneous into it; furthermore, the probability current $\mathbf{J}(z,x)$ for $z < 0$ is not always vertical along the $(-x)$ axis, unlike Figs. 6(a), 6(b), and 6(d). The transmission is again negligible both for the normal incidence [$\theta = 0$, Fig. 7(a)] and for directions close to the ideal angle [$\theta = \theta_0 \pm 2^\circ$, Figs. 7(b) and 7(d)]. In contrast, when $\theta = \theta_0$ [Fig. 7(c)], the result is almost flawless and identical to that of Fig. 6(c), a feature indicating once again the extreme directional preference of the investigated geometry regardless of the type of resonance it supports.

It must be noted that not only the squared magnitude of the wave function $\Psi(z,x)$ has a physical meaning but also its real and imaginary parts are functions employed in quantum signal processing [57,58] and computing [59]. Therefore, in Fig. 8, we depict the signal $\mathrm{Re}[\Psi(z,x)]$ for two characteristic optimal designs as a function of position z (along a fixed line $x = 0$). In Fig. 8(a), we consider an InP inclusion hosted by InAs, optimized for particles of $E = 1$ eV and excited by e beams of various orientations θ. The design supports Fabry-Perot resonance and, as expected, is transparent to the impinging matter wave when $\theta = \theta_n$, while practically impenetrable for all the other angles, even those very close $(\pm 3^\circ)$ to θ_n. Importantly, the matching is achieved via half oscillation of $\mathrm{Re}[\Psi]$ into the slab; its variation is more rapid for smaller θ and much milder, resembling an evanescent instead of propagating wave, once $\theta > \theta_n$. Note also that the $\mathrm{Re}[\Psi]$ can take large amplitudes into the filter when the e beam is blocked but is bounded by unity for the passing θ. In addition, the wave for $z < 0$ always respects the inequality $|\mathrm{Re}[\Psi]| < 2$ since reflection coefficient cannot surpass unity in passive configurations. In Fig. 8(b), we regard a design (InSb slab hosted by diamond) optimized for energy level $E = 0.5$ eV that maintains a trivial resonance. The wave function $\mathrm{Re}[\Psi]$ is kept constant and the tunneling for

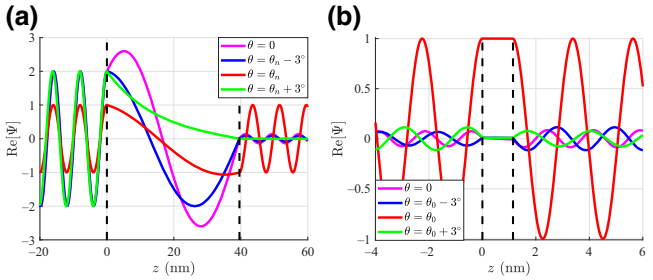

FIG. 8. Spatial distribution of the quantum signal $\mathrm{Re}[\Psi(z,x)]$ as a function of the position z (at fixed $x = 0$) for the (a) InP slab hosted by InAs (Fabry-Perot resonance, $\theta_n \cong 8.1°$, $1/\bar{\tau} \cong 270$, $E = 1$ eV) and (b) InSb slab hosted by diamond (trivial resonance, $\theta_0 \cong 39.6°$, $1/\bar{\tau} \cong 88$, $E = 0.5$ eV) for various angles of incidence θ. Dashed lines denote the boundaries of the quantum filter.

$\theta = \theta_0$ is performed by bridging the two unitary-oscillating waves; importantly, when $\theta \neq \theta_0$, $\mathrm{Re}[\Psi]$ possesses very low values revealing an almost total and opposite-phase reflection for $z < 0$.

In Fig. 9, we consider the same designs as in Fig. 8 but we represent $|\Psi(z,x)|^2$ in dB for a continuous range of directions θ around the optimal ones. In Fig. 9(a), where Fabry-Perot resonance is hosted by a quantum-barrier configuration, we notice the absence of reflections when $\theta = \theta_n$ and the huge magnitudes of wave function into the slab in the vicinity of the optimal angle. The shift of the single minimum of $|\Psi|^2$ within the planar inclusion towards smaller $0 < z < h$ (once θ increases) should also be noted. In Fig. 9(b), where trivial resonance occurs at a deep quantum-well setup, one directly observes that the represented quantity is bounded by unity, as happens in Fig. 8(b). Finally, the spatial oscillations for increasing θ are slower because the slab "feels" a periodic excitation of larger period along the tangential direction; in contrast, the variation of $|\Psi(z,x)|^2$ is negligible when $\theta \cong \theta_0$.

To manifest further the efficiency of our designs, we pick one (investigated in Fig. 7, namely the InSb cavity in diamond with $E = 1$ eV) in order to examine it in the presence of all possible rays instead of a specific matter

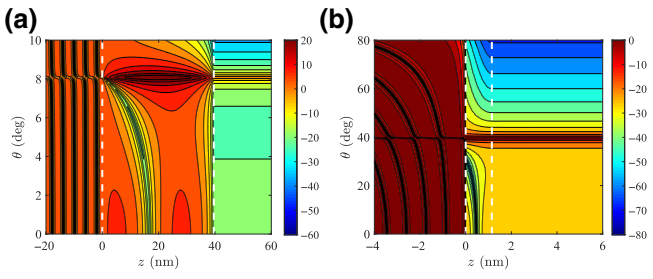

FIG. 9. Spatial distribution of $|\Psi(z,x)|^2$ in dB as a function of the position z (for fixed x) across a continuous spectrum of incidence angle θ for the same designs of Fig. 8.

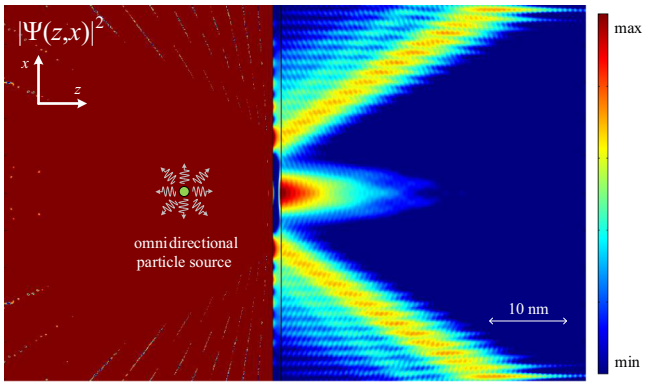

FIG. 10. Spatial distribution of the probability $|\Psi(z,x)|^2$ across the optimal InSb configuration in diamond under the excitation of cylindrical source of particles with $E = 1$ eV (trivial resonance reported at Table II and considered by Fig. 7).

plane wave. Therefore, in Fig. 10 we assume a cylindrical beam of particles (omnidirectional source), emitting electrons along all directions with equal probability, in the vicinity of the optimal slab with $\theta_0 \cong 27.2°$. A quantity proportional to $|\Psi(z,x)|^2$ is computed and represented with help from commercial software COMSOL Multiphysics [60]. We record huge reflections from the slab as the vast majority of the incident rays are almost 100% reflected; however, a normally incident wave manages to partially penetrate through the filter since always $\tau(0) \neq 0$ and additionally because it has the shortest path to cover. Most importantly, the beams with $\theta = \pm\theta_0$ almost entirely pass to the other side with magnitudes of $\Psi(z,x)$ much larger than the corresponding one of $\theta = 0$, as z increases. In this way, the extreme directional selectivity of the reported configurations in e-beam tunneling is fully demonstrated, while the ability of the corresponding designs to abruptly switch their response if a specific angle is excited, is shown.

D. Sensitivity to fabrication and engineering defects

Recent advances in the thin-film industry and technology [61] have allowed the construction of layers of semiconductors in the range of a few nanometers [12,15], thus rendering realizable all these extremely small slabs presented in our study (like those in Tables I and II). In particular, chemical deposition methods use a fluid precursor that goes through a chemical change across a surface, resulting in a solid slab. These layers tend to be conformal films, meaning that the thickness of the layer is ideally the same everywhere along the interface, or that the thickness deviations are minimal. Indeed, chemical vapor deposition is a well-established chemical process employed to produce high-quality solid thin-film coatings [19] on substrates [22]. In addition, there are available various physical deposition methods like lithographic etching [30]

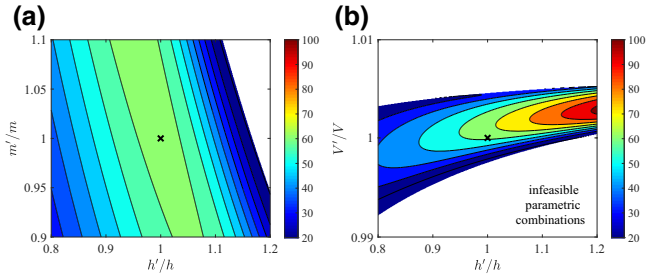

FIG. 11. Variation of (inverse) average transmissivity $1/\bar{\tau}$ as a function of miscalculated slab thickness h'/h and (a) inaccurate effective mass m'/m in the slab, (b) inaccurate potential energy V'/V in the slab. CdO filter in AlSb environment for $E = 0.5$ eV [Fabry-Perot resonance included in Fig. 2(b)]. Black $\times$ marks the proposed operation point ($1/\bar{\tau} \cong 62$, $\theta_n \cong 11.1^\circ$). Blank regions correspond to parametric combinations not leading to exactly one direction of 100% transmission. Plot parameters, $V_0 \cong 2.27$ eV, $V \cong 2.16$ eV, $h \cong 18.7$ nm.

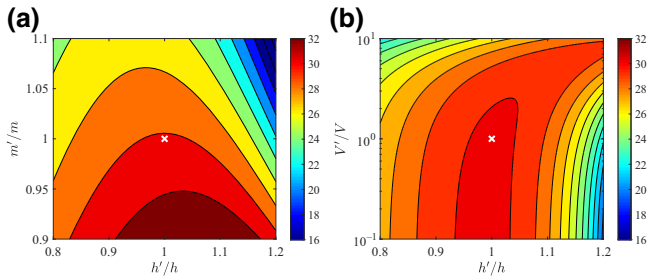

FIG. 12. The same as in Fig. 11 for the InAs filter in BN and $E = 1$ eV [trivial resonance shown in Fig. 2(c), included in Table II]. White $\times$ marks the proposed operation point ($1/\bar{\tau} \cong 30$, $\theta_0 \cong 31.4^\circ$). Plot parameters, $V_0 \cong 7.90$ eV, $V \cong 0.36$ eV, $h \cong 1.03$ nm.

and molecular beam epitaxy that is a renowned, notably precise but rather costly fabrication technique [10]. It takes place in high vacuum and involves directed neutral thermal atomic and molecular beams that impinge on a heated substrate [16,23].

However, finesse in design should not be taken for granted especially since the slightest imperfection can harm the particularly fragile quantum effects and their reliable recording [62] by creating decoherence or effective noise. Therefore, it is useful to examine the behavior of the suggested filters when their size h is not perfectly fabricated or their texture (m, V) becomes inaccurately engineered due to unwanted inclusions. Accordingly, we assume in this subsection that the particles of specific energy E travel as matter plane waves into the background host with exactly determined effective quantities (m_0, V_0) and investigate the effect of misselecting the rest of the setup parameters, namely film thickness $h' \neq h$, effective mass $m' \neq m$, and potential level $V' \neq V$ in the slab.

In Fig. 11, we consider a layout sustaining Fabry-Perot interference at $E = 0.5$ eV [from Fig. 2(b)] and represent the metric $1/\bar{\tau}$ as a function of h'/h; in particular, in Fig. 11(a), we examine its variation on the $(h'/h, m'/m)$ map. The blank regions indicate parametric combinations not permitting exactly one resonance for $0 < \theta < 90^\circ$, similar to those of blue regions in the existence map of Fig. 1(c). It is clear that the robustness of the performance is higher with respect to inaccurate effective mass estimation than in the case of imperfect forming of the cavity. However, the score is kept quite high for $0.9 < h'/h < 1.1$ even though it drops more rapidly for larger than the optimal thicknesses. Note also that if both effective mass and size take higher values, the structure does not serve its purpose anymore as a filter of a single direction. In Fig. 11(b) we investigate the variation of $1/\bar{\tau}$ on the $(h'/h, V'/V)$ plane, while keeping $m' = m$. Since the design constitutes a very shallow potential well ($V \cong V_0$), the response is very sensitive to changes of the potential; as a result, even the slightest change can send us to an infeasible setup; however, the device exhibits substantial endurance with respect to the width of the slab and, most importantly, may increase its performance for thicker structures. These better designs for the same V are not detected by the adopted optimization scheme since we search the maximum of $1/\bar{\tau}$ within the interval $0 < h/\lambda < 5$; thus, the reported scores can be enhanced further if larger h/λ ranges are considered and nonboundary extrema constraints [63,64] are imposed (the filter of Fig. 11 has thickness $h/\lambda = 5$).

In Fig. 12, we consider a totally different design based on the trivial resonance that employs a huge contrast between potential energy in slab V and background V_0. In Fig. 12(a), one observes that the level of $1/\bar{\tau}$ is retained despite the significant deviations from the proposed values; furthermore, the highest scores are attainable for smaller effective masses; unlike in Fig. 11(b), such maxima are not accessible through the followed maximization process since m is not a free parameter but takes only distinct values according to the list of available media. In Fig. 12(b) we regard again the $(h'/h, V'/V)$ map and realize that, despite the considerable variation of potential (by 2 orders of magnitude), the performance of the device is not affected much since $V_0 \gg V$ meaning that the value of V plays little role; for the same reason, we do not see blank areas in both panels of Fig. 12. Therefore, one can clearly understand that the designs employing very deep quantum wells (upper left portion of panels in Fig. 2) are much less vulnerable to fabrication and engineering defects than the ones working for $V \cong V_0$ (diagonal of panels in Fig. 2), regardless of the type of resonance.

IV. CONLUSIONS

Classical electromagnetics and quantum mechanics deal mostly with waves that obey similar dynamic laws; therefore, they mutually share several concepts and techniques. Given the huge recent upsurge of funding and

industrial interest for quantum engineering combined with the fact that electrodynamics is the older of the two scientific branches, it is quite common to see photonic ideas translated into the quantum arena. The well-known Fabry-Perot resonator providing transmissivity control based on the interference of reflections makes an example of an architecture, initially introduced for electromagnetic waves, that describe well the matter-wave interactions in quantum-well and barrier configurations. In this study, we excite obliquely such a planar slab with an impinging electron beam traveling into a specific background and search for optimal combinations of sizes and materials giving directionally selective tunneling. After an exhaustive, trial-and-error search through an arbitrarily long list of available quantum media, sets of filter designs are found to permit transmission only of those particles incoming at a particular angle. Such an extreme directional preference is demonstrated for several levels of energies, while the robustness of the performance in the presence of various construction defects is also examined.

In this regard, a database of ultra-selective directional quantum filters is populated offering extra degrees of freedom in modeling and fabrication. At the same time, such a library contains the highest selectivity scores that can be hit by our simple layout when employing the considered set of materials; more substantial performances may be accomplished only with the use of more complicated multilayered structure or more sophisticated anisotropic texture. The same process can be expanded to setups of increased complexity, where the heavier optimizations will be executed via state-of-the-art inverse design algorithms [65–67], to provide ultra-performing configurations for a much broader range of quantum-engineering applications.

ACKNOWLEDGMENTS

The author would like to thank Professor Efthimios Kaxiras (Harvard University, MA, USA), Professor Dieter Suter (Technical University of Dortmund, Germany), Professor Christophe Berthod (University of Geneva, Switzerland) and Dr. Marios Mattheakis (Harvard University, MA, USA) for useful discussions regarding the quantum properties of considered materials.

This work was partially supported by Nazarbayev University Faculty Development Competitive Research Grant No. 090118FD5349 (*"Super transmitters, radiators and lenses via photonic synthetic matter"*). Funding from MES RK state-targeted program BR05236454 is also acknowledged.

[1] Ø. Fischer, M. Kugler, I. Maggio-Aprile, and C. Berthod, Scanning tunneling spectroscopy of high-temperature superconductors, Rev. Mod. Phys. **79**, 353 (2007).

[2] C. L. Degen, F. Reinhard, and P. Cappellaro, Quantum sensing, Rev. Mod. Phys. **89**, 035002 (2017).

[3] H. Mabuchi and A. C. Doherty, Cavity quantum electrodynamics: Coherence in context, Science **298**, 1372 (2002).

[4] C. Clausen, I. Usmani, F. Bussières, N. Sangouard, M. Afzelius, H. de Riedmatten, and N. Gisin, Quantum storage of photonic entanglement in a crystal, Nature **469**, 508 (2011).

[5] H. J. Kimble, The quantum internet, Nature **453**, 1023 (2008).

[6] *National Quantum Initiative Act*, Act of 115th US Congress, Passed: December 13 (2018).

[7] *NSF-ANR Partnership for International Research and Education in Hybrid Materials for Quantum Science and Engineering*, PIRE:HYBRID, http://pirehybrid.org/pirehybrid.org/, Director: S. Frolov, University of Pittsburgh (2017).

[8] 2016 US Department of Defense MURI Awards, *Quantum Materials by Design with Electromagnetic Excitation*, ARO MURI W911NF-16-1-0361, PI: D. Hsieh, (2016).

[9] 2018 US Department of Defense MURI Awards, *Ab-Initio Solid-State Quantum Materials: Design, Production, and Characterization at the Atomic Scale*, ARO MURI W911NF-18-1-0432, PI: D. Englund (2018).

[10] T. C. L. G. Sollner, P. E. Tannenwald, D. D. Peck, and W. D. Goodhue, Quantum well oscillators, Appl. Phys. Lett. **45**, 1319 (1984).

[11] R. J. Simes, R. H. Yan, R. Geels, L. A. Coldren, J. H. English, and A. C. Gossard, Fabry-Perot multiple-quantum well index modulator, Appl. Opt. **27**, 2103 (1988).

[12] M. Whitehead and G. Parry, High-contrast reflection modulation at normal incidence in asymmetric multiple quantum well Fabry-Perot structure, Electron. Lett. **25**, 566 (1989).

[13] D. A. B. Miller, Quantum well optoelectronic switching devices, Int. J. High Speed Electron. Syst. **1**, 19 (1990).

[14] C. Valagiannopoulos and P. G. Lagoudakis, Photonic crystals for optimal color conversion in light-emitting diodes: A semi-analytical approach, J. Opt. Soc. Am. B **35**, 1105 (2018).

[15] J. Miguel-Sánchez, A. Reinhard, E. Togan, T. Volz, A. Imamoglu, B. Besga, J. Reichel, and J. Estève, Cavity quantum electrodynamics with charge-controlled quantum dots coupled to a fiber Fabry-Perot cavity, New J. Phys. **15**, 045002 (2013).

[16] J. E. Roth, O. Fidaner, R. K. Schaevitz, Y.-H. Kuo, T. I. Kamins, J. S. Harris, and D. A. B. Miller, Optical modulator on silicon employing germanium quantum wells, Opt. Express **15**, 5851 (2007).

[17] D. D. Marcenac and J. E. Carroll, Quantum-mechanical model for realistic Fabry-Perot lasers, IEE Proc. J. **140**, 157 (1993).

[18] M. Paternostro, M. S. Kim, and B. S. Ham, Generation of entangled coherent states via cross-phase-modulation in a double electromagnetically induced transparency regime, Phys. Rev. A **67**, 023811 (2003).

[19] F. De Martini, M. Marrocco, P. Mataloni, L. Crescentini, and R. Loudon, Spontaneous emission in the optical microscopic cavity, Phys. Rev. A **43**, 2480 (1991).

[20] S. M. Dutra and P. L. Knight, Spontaneous emission in a planar Fabry-Perot microcavity, Phys. Rev. A **53**, 3587 (1996).

[21] J. M. Vaughan, *The Fabry-Perot Interferometer: History, Theory, Practice and Applications* (Taylor & Francis, New York, New York, USA, 1989).

[22] F. Capasso, K. Mohammed, and A. Cho, Resonant tunneling through double barriers, perpendicular quantum transport phenomena in superlattices, and their device applications, IEEE J. Quantum Electron. **22**, 1853 (1986).

[23] F. Capasso, S. Sen, F. Beltram, L. M. Lunardi, A. S. Vengurlekar, P. R. Smith, N. J. Shah, R. J. Malik, and A. Y. Cho, Quantum functional devices: Resonant-tunneling transistors, circuits with reduced complexity, and multiple-valued logic, IEEE Trans. Electron Dev. **36**, 2065 (1989).

[24] C. Sirtori, F. Capasso, J. Faist, A. L. Hutchinson, D. L. Sivco, and A. Y. Cho, Resonant tunneling in quantum cascade lasers, IEEE J. Quantum Electron. **34**, 1722 (1998).

[25] E. H. Hauge and J. A. Støvneng, Tunneling times: A critical review, Rev. Mod. Phys. **61**, 917 (1989).

[26] E. H. Hauge, J. P. Falck, and T. A. Fjeldly, Transmission and reflection times for scattering of wave packets off tunneling barriers, Phys. Rev. B **36**, 4203 (1987).

[27] M. Ley and R. Loudon, Quantum theory of high-resolution length measurement with a Fabry-Perot interferometer, J. Mod. Opt. **34**, 227 (1987).

[28] X. P. Feng and K. Ujihara, Quantum theory of spontaneous emission in a one-dimensional optical cavity with two-side output coupling, Phys. Rev. A **41**, 2668 (1990).

[29] S. Ataman, The quantum optical description of a Fabry-Perot interferometer and the prediction of an antibunching effect, Eur. Phys. J. D **69**, 187 (2015).

[30] G. H. Henderson, L. C. West, T. K. Gaylord, C. W. Roberts, E. N. Glytsis, and M. T. Asom, Semiconductor devices based on optical transitions between quasibound energy levels, U.S. Patent No. 08/011010, 5386126 (1995).

[31] F. Fratini, E. Mascarenhas, L. Safari, J-Ph. Poizat, D. Valente, A. Auffèves, D. Gerace, and M. F. Santos, Fabry-Perot Interferometer with Quantum Mirrors: Nonlinear Light Transport and Rectification, Phys. Rev. Lett. **113**, 243601 (2014).

[32] Y. Shen, D. Ye, I. Celanovic, S. G. Johnson, J. D. Joannopoulos, and M. Soljačić, Optical broadband angular selectivity, Science **343**, 1499 (2014).

[33] J. Y. Lee and R.-K. Lee, Hiding the interior region of core-shell nanoparticles with quantum invisible cloaks, Phys. Rev. B **89**, 155425 (2014).

[34] J. Y. Lee, A. E.Miroshnichenko, and R.-K. Lee, Designing quantum resonant scatterers at subwavelength scale, Phys. Lett. A **381**, 2860 (2017).

[35] C. Valagiannopoulos, Maximal quantum scattering by homogeneous spherical inclusions, Phys. Rev. B **100**, 035308 (2019).

[36] R. Fleury and A. Alù, Manipulation of electron flow using near-zero index semiconductor metamaterials, Phys. Rev. B **90**, 035138 (2014).

[37] T. Ogawana and H. Sakaguchi, Transmission coefficient from generalized cantor-like potentials and its multifractality, Phys. Rev. E **97**, 012205 (2018).

[38] S. Adachi, *Properties of Semiconductor Alloys: Group-IV, III–V and II–VI Semiconductors* (John Wiley & Sons, New York, New York, USA, 2009).

[39] E. Kaxiras and J. D. Joannopoulos, *Quantum Theory of Materials* (Cambridge University Press, New York, New York, USA, 2019).

[40] S. Trachanas, *An Introduction to Quantum Physics* (John Wiley & Sons, New York, New York, USA, 2018).

[41] D. J. Griffiths, *Introduction to Quantum Mechanics* (Pearson Prentice Hall, Upper Saddle River, New Jersey, USA, 2005).

[42] M. Gring, M. Kuhnert, T. Langen, T. Kitagawa, B. Rauer, M. Schreitl, I. Mazets, D. A. Smith, E. Demler, and J. Schmiedmayer, Relaxation and prethermalization in an isolated quantum system, Science **337**, 1318 (2012).

[43] M. Aidelsburger, M. Atala, M. Lohse, J. T. Barreiro, B. Paredes, and I. Bloch, Realization of the Hofstadter Hamiltonian with Ultracold Atoms in Optical Lattices, Phys. Rev. Lett. **111**, 185301 (2013).

[44] K. J. Savage, M. M. Hawkeye, R. Esteban, A. G. Borisov, J. Aizpurua, and J. J. Baumberg, Revealing the quantum regime in tunneling plasmonics, Nature **491**, 574 (2012).

[45] G. Feve, A. Mahe, J.-M. Berroir, T. Kontos, B. Placais, D. C. Glattli, A. Cavanna, B. Etienne, and Y. Jin, An on-demand coherent single electron source, Science **316**, 1169 (2007).

[46] J. P. Pekola, O.-P. Saira, V. F. Maisi, A. Kemppinen, M. Möttönen, Yu. A. Pashkin, and D. V. Averin, Single-electron current sources: Toward a refined definition of the ampere, Rev. Mod. Phys. **85**, 1421 (2013).

[47] M. S. Tame, K. R. McEnery, S. K. Özdemir, J. Lee, S. A. Maier, and M. S. Kim, Quantum plasmonics, Nat. Phys. **9**, 329 (2013).

[48] J. M. Fitzgerald. P. Narang, R. V. Craster, S. A. Maier, and V. Giannini, Quantum plasmonics, Proc. IEEE **104**, 2307 (2016).

[49] Y. Liu and A. A. Houck, Quantum electrodynamics near a photonic bandgap, Nat. Phys. **13**, 48 (2017).

[50] C. Fares, M. J. Tadjer, J. Woodward, N. Nepal, M. A. Mastro, C. R. Eddy, Jr., F. Ren, and S. J. Pearton, Valence and conduction band offsets for inN and III-nitride ternary alloys on (−201) bulk β-Ga_2O_3, ECS J. Solid State Sci. Technol. **8**, Q3154 (2019).

[51] E. P. Shapera and A. Schleife, Database-driven materials selection for semiconductor heterojunction design, Adv. Theory Simul. **1**, 1800075 (2018).

[52] S. Savoia, G. Castaldi, V. Galdi, A. Alù, and N. Engheta, Tunneling of obliquely incident waves through PT-symmetric epsilon-near-zero bilayers, Phys. Rev. B **89**, 085105 (2014).

[53] G. Beuermann, On the directional selectivity of tunneling experiments, Z. Phys. B **44**, 29 (1981).

[54] M. Mattheakis, C. A. Valagiannopoulos, and E. Kaxiras, Epsilon-near-zero behavior from plasmonic dirac point: Theory and realization using two-dimensional materials, Phys. Rev. B **94**, 201404(R) (2016).

[55] R. Schirhagl, K. Chang, M. Loretz, and C. L. Degen, Nitrogen-vacancy centers in diamond: Nanoscale sensors for physics and biology, Annu. Rev. Phys. Chem. **65**, 83 (2014).

[56] J. R. Maze, PhD Dissertation, Harvard University, Cambridge, Massachusetts, USA (2010).

[57] F. Krausz and M. I. Stockman, Attosecond metrology: From electron capture to future signal processing, Nat. Photonics **8**, 205 (2014).

[58] J. Wang, J.-Y. Yang, I. M. Fazal, N. Ahmed, Y. Yan, H. Huang, Y. Ren, Y. Yue, S. Dolinar, M. Tur, and A. E. Willner, Terabit free-space data transmission employing orbital angular momentum multiplexing, Nat. Photonics **6**, 488 (2012).

[59] H. P. Specht, C. Nölleke, A. Reiserer, M. Uphoff, E. Figueroa, S. Ritter, and G. Rempe, A single-atom quantum memory, Nature **473**, 190 (2011).

[60] COMSOL Multiphysics® v. 5.4, www.comsol.com COMSOL AB, Stockholm, Sweden (2019).

[61] K. Seshan, *Handbook of Thin Film Deposition: Techniques, Processes, and Technologies* (Elsevier, New York, New York, USA, 2012).

[62] A. Kandala, K. Temme, A. D. Córcoles, A. Mezzacapo, J. M. Chow, and J. M. Gambetta, Error mitigation extends the computational reach of a noisy quantum processor, Nature **567**, 491 (2019).

[63] A. Abrashuly and C. Valagiannopoulos, Limits for Absorption and Scattering by Core-Shell Nanowires in the Visible Spectrum, Phys. Rev. Appl. **11**, 014051 (2019).

[64] A. Sheverdin and C. Valagiannopoulos, Core-shell nanospheres under visible light: Optimal absorption, scattering, and cloaking, Phys. Rev. B **99**, 075305 (2019).

[65] O. D. Miller, PhD Dissertation, University of California, Berkeley, California, USA (2013).

[66] S. Molesky, Z. Lin, A. Y. Piggott, W. Jin, J. Vuckovic, and A. W. Rodriguez, Outlook for inverse design in nanophotonics, Nat. Photonics **12**, 659 (2018).

[67] J. Peurifoy, Y. Shen, L. Jing, Y. Yang, F. Cano-Renteria, B. G. DeLacy, J. D. Joannopoulos, M. Tegmark, and M. Soljačić, Nanophotonic particle simulation and inverse design using artificial neural networks, Sci. Adv. **4**, eaar4206 (2018).